The mechanism of vortex instability in electromagnetically driven flow in an annular thin layer of electrolyte

J. McCloughan[1] S. A. Suslov[2]

(Received 8 March 2020; revised 1 July 2020)

Abstract

A circumferential flow of a conducting fluid in an annular channel can be created by the action of a Lorentz force arising as a result of the interaction between an applied vertical magnetic field and a radial electric current flowing through the electrolyte. Quite unexpectedly, experiments revealed that a robust vortex system appears near the outer cylindrical wall in such flows. McCloughan and Suslov (J. Fluid Mech. 887:A23, 2020) (McCS) reported comprehensive linear stability results of such a flow for variable Lorentz forcing. Here we complement that study by investigating the flow structure as a function of the channel aspect ratio. Remarkably, despite the completely different physical nature of parametric dependences, dynamic in McCS and

DOI:10.21914/anziamj.v61i0.15168, © Austral. Mathematical Soc. 2020. Published 2020-08-20, as part of the Proceedings of the 14th Biennial Engineering Mathematics and Applications Conference. ISSN 1445-8810. (Print two pages per sheet of paper.) Copies of this article must not be made otherwise available on the internet; instead link directly to the DOI for this article.

purely geometric here, we show that in both scenarios vortices appear on a background of a steady axisymmetric flow at the boundary between two counter-rotating toroidal structures and have a similar energy distributions. The two studies demonstrate the robustness of the mechanism responsible for the vortex formation: Rayleigh's inviscid centrifugal instability aided by radial shear in the boundary layer near the outer cylindrical wall.

Contents

1 Introduction and problem formulation C215

2 Steady axisymmetric basic flow solutions C218

3 Linear stability analysis C221

1 Introduction and problem formulation

Rotating magnetohydrodynamic flows of liquid metals and electrolytes are of interest across various research fields and in many industrial applications, such as stirring. In laboratory studies of geophysical, atmospheric and astrophysical phenomena, electromagnetic forces are often used to drive the flow of a conducting model fluid. When such a fluid is confined between two vertical coaxial cylindrical electrodes and placed into a vertical magnetic field $\mathbf{B}$, a Lorentz force $\mathbf{F_L} = \mathbf{j} \times \mathbf{B}$, where $\mathbf{j}$ is electric current density, arises and drives the fluid circumferentially. Experiments show that, quite unexpectedly, a robust system of vortices arises near the outer cylindrical wall [3]. McCloughan and Suslov [2] (referred to as McCS below) showed that these vortex systems appeared when the applied current across the cavity exceeded a certain threshold. In the current article we investigate the system behaviour when the electrolyte depth (channel aspect ratio), rather than the current, is varied.

Figure 1: Sketch of the problem geometry. The circumferentially moving electrolyte is contained in a layer of depth $\mathfrak{h}$ between two vertical cylindrical electrodes located at $\mathfrak{r}^* = \mathfrak{R}_1$ and $\mathfrak{r}^* = \mathfrak{R}_2$ (stars denote dimensional quantities). A disk magnet underneath the layer generates a predominantly vertical magnetic field with magnitude $\mathfrak{B}_0$ at the inner corner of the channel.

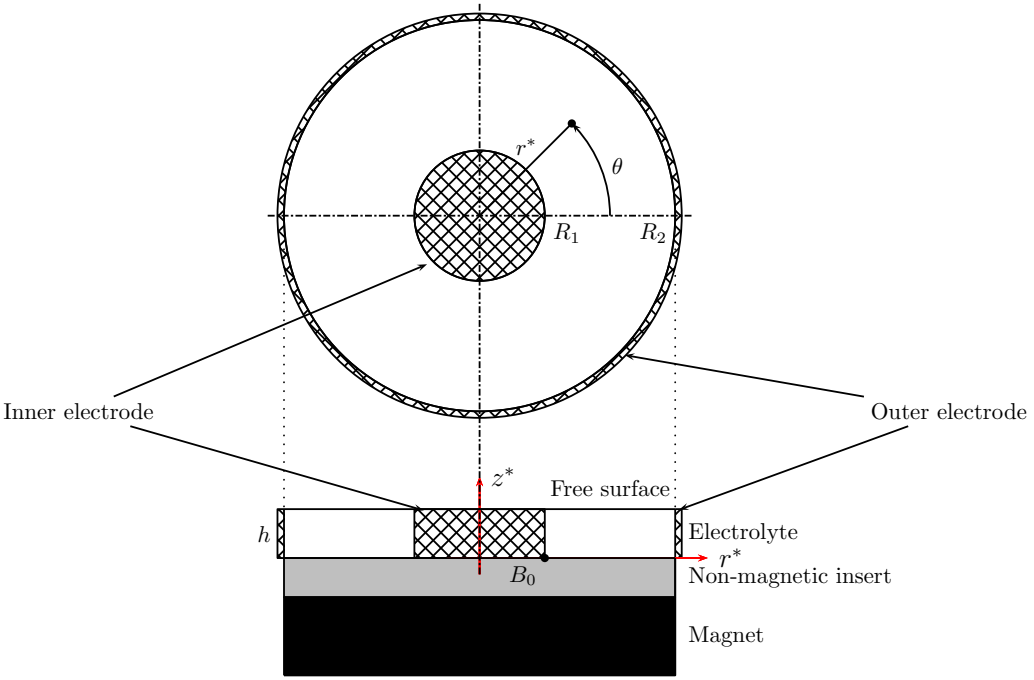

Consider a layer of incompressible viscous electrolyte of thickness $\mathfrak{h}$, confined to an annular channel formed by two vertical co-axial cylindrical electrodes of radius $\mathfrak{R}_1$ and $\mathfrak{R}_2$, $\mathfrak{R}_1 < \mathfrak{R}_2$, as shown in Figure 1. The bottom of the cavity is solid and non-conducting, while the top is a free surface. The electrolyte has dynamic viscosity μ, density ρ and electric conductivity σ_e. This system is placed above a permanent disk magnet that creates a predominantly vertical magnetic field characterised by the amplitude $\mathfrak{B}_0$ in the corner between the inner electrode and the solid bottom, that is, at $(\mathfrak{r}^*, z^*) = (\mathfrak{R}_1, 0)$.

Under the small magnetic Reynolds number approximation [1] the magnetic field generated by the flowing electrolyte is negligible compared to that of the magnet. Therefore, the steady axisymmetric non-dimensional Poisson's equation for the electric potential ϕ, and the momentum and continuity equations for an incompressible fluid written in scaled cylindrical coordinates become [2]

$$\frac{\partial^2\phi}{\partial z^2} + \epsilon^2\left(\frac{\partial^2\phi}{\partial r^2} + \frac{1}{r}\frac{\partial\phi}{\partial r}\right) = \epsilon^2 Ha^2\left[-B_r\frac{\partial v}{\partial z} + B_z\left(\frac{\partial v}{\partial r} + \frac{u_\theta}{r}\right)\right], \tag{1}$$

$$u\frac{\partial u}{\partial r} - \frac{v^2}{r} + w\frac{\partial u}{\partial z} = -\frac{\partial p}{\partial r} + \frac{1}{\epsilon^2 Re}j_\theta B_z + \frac{1}{Re}\left(\frac{\partial^2 u}{\partial r^2} + \frac{1}{r}\frac{\partial u}{\partial r} - \frac{u}{r^2} + \frac{1}{\epsilon^2}\frac{\partial^2 u}{\partial z^2}\right), \tag{2}$$

$$u\frac{\partial v}{\partial r} + \frac{uv}{r} + w\frac{\partial v}{\partial z} = \frac{1}{\epsilon^2 Re}\left(j_z B_r - j_r B_z\right) + \frac{1}{Re}\left(\frac{\partial^2 v}{\partial r^2} + \frac{1}{r}\frac{\partial v}{\partial r} - \frac{v}{r^2} + \frac{1}{\epsilon^2}\frac{\partial^2 v}{\partial z^2}\right), \tag{3}$$

$$u\frac{\partial w}{\partial r} + w\frac{\partial w}{\partial z} = -\frac{1}{\epsilon^2}\frac{\partial p}{\partial z} - \frac{1}{\epsilon^2 Re}j_\theta B_r + \frac{1}{Re}\left(\frac{\partial^2 w}{\partial r^2} + \frac{1}{r}\frac{\partial w}{\partial r} + \frac{1}{\epsilon^2}\frac{\partial^2 w}{\partial z^2}\right), \tag{4}$$

$$\frac{\partial u}{\partial r} + \frac{u}{r} + \frac{\partial w}{\partial z} = 0\,. \tag{5}$$

with corresponding boundary conditions

$$u = v = w = 0 \quad \text{at } z = -1 \text{ and at } r = \alpha \pm 1\,, \tag{6}$$

$$w = \frac{\partial u}{\partial z} = \frac{\partial v}{\partial z} = 0 \quad \text{at } z = 1\,, \tag{7}$$

$$\phi = 0 \quad \text{at } r = \alpha - 1\,, \quad \text{and} \quad \phi = 1 \quad \text{at } r = \alpha + 1\,, \tag{8}$$

$$\frac{\partial\phi}{\partial z} = 0 \quad \text{at } z = -1\,, \quad \text{and} \quad \frac{\partial\phi}{\partial z} = -\epsilon^2 Ha^2 v B_r \quad \text{at } z = 1\,, \tag{9}$$

where $r = \frac{r^*}{R_2 - R_1}$, $z = \frac{z^*}{h}$ are the scaled coordinates, p is the pressure including the hydrostatic component, $\mathbf{u} = u\boldsymbol{e}_r + v\boldsymbol{e}_\theta + w\boldsymbol{e}_z$ and $\mathbf{B} = B_r\boldsymbol{e}_r + B_z\boldsymbol{e}_z$ are the velocity and magnetic fields, respectively, with subscripts indicating components in the radial (r), circumferential (θ) and vertical (z) directions. From Ohm's law, the electric current density is

$$\begin{aligned} \mathbf{j} &= \left(-\frac{\partial \phi}{\partial r} + \mathrm{Ha}^2 v B_z\right)\boldsymbol{e}_r + \mathrm{Ha}^2\left(\epsilon^2 w B_r - u B_z\right)\boldsymbol{e}_\theta \\ &= -\left(\frac{\partial \phi}{\partial z} + \epsilon^2 \mathrm{Ha}^2 v B_r\right)\boldsymbol{e}_z\,. \end{aligned} \tag{10}$$

The non-dimensional parameters describing the flow are the aspect ratio of the fluid layer ϵ, the square of Hartmann number Ha^2 characterising electromagnetic effects and Reynolds number Re quantifying the ratio of the Lorentz and viscous forces:

$$\epsilon = \frac{h}{R_2 - R_1}, \quad \mathrm{Ha}^2 = \frac{\sigma_e B_0^2 h^2}{4\mu}, \quad \mathrm{Re} = \frac{\rho U_0 (R_2 - R_1)}{2\mu}, \tag{11}$$

where σ_e is the electrical conductivity, μ is the dynamic viscosity, ρ is the mass density, and the velocity scale and the geometric parameter are defined, respectively, as

$$U_0 = \frac{\sigma_e \Delta\phi_0 B_0 h}{2\mu}\epsilon \quad \text{and} \quad \alpha = \frac{R_2 + R_1}{R_2 - R_1}, \tag{12}$$

where $\Delta\phi_0$ is the electric potential difference applied between the electrodes.

2 Steady axisymmetric basic flow solutions

As described by Suslov, Pérez-Barrera, and Cuevas [4], the primary circumferential fluid motion results in a centrifugal force responsible for the creation of a radial velocity component so that the overall flow becomes toroidal. Suslov, Pérez-Barrera, and Cuevas [4] referred to such a flow as Type 1. It is illustrated in Figure 2(a, b).

Figure 2: The steady axisymmetric basic flow solutions for $\epsilon = \epsilon_* = 0.219$, $\mathrm{Ha} = 4.47 \times 10^{-3}$ and $\mathrm{Re} = 1177$. Panels (a, b) and (c, d) show the Type 1 and 2 solutions, respectively. The red (blue) regions in panels (a, c) correspond to large (small) circumferential velocity v and in panels (b, d) to positive (negative) circumferential vorticity component $\omega_\theta = \frac{1}{\epsilon}\frac{\partial u}{\partial z} - \epsilon\frac{\partial w}{\partial r}$.

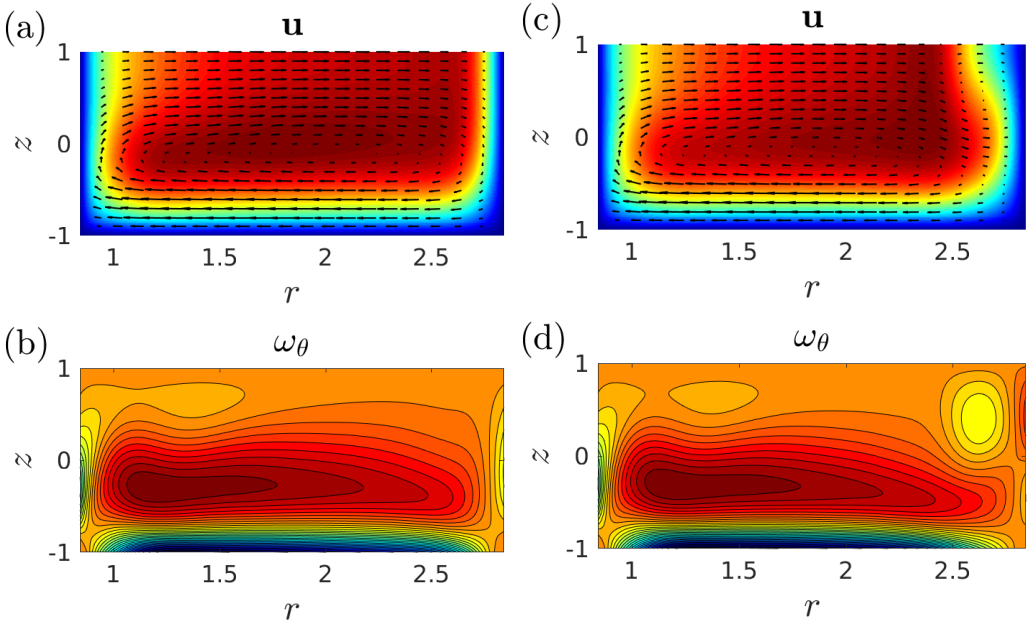

If the aspect ratio ϵ is increased while the product $\Delta\phi_0 h$ of the applied potential difference and the thickness of the layer remains constant (as explained by McCS this corresponds to experiments with fixed total current flowing between the electrodes), then a second axisymmetric solution, referred to as Type 2, appears at some aspect ratio value $\epsilon = \epsilon_*$. This solution is illustrated in Figure 2(c, d). The main feature that distinguishes Type 1 and Type 2 solutions is a secondary counter-rotating toroidal structure near the free surface and the outer wall. This toroidal structure creates a counter flow near the free surface with a stagnation point at some distance from the outer wall. Even though Type 2 solutions are caused by a purely geometric effect

Figure 3: Same as Figure 2 but for $\epsilon = 0.258$, $\mathrm{Ha} = 5.28 \times 10^{-3}$ and $\mathrm{Re} = 1391$.

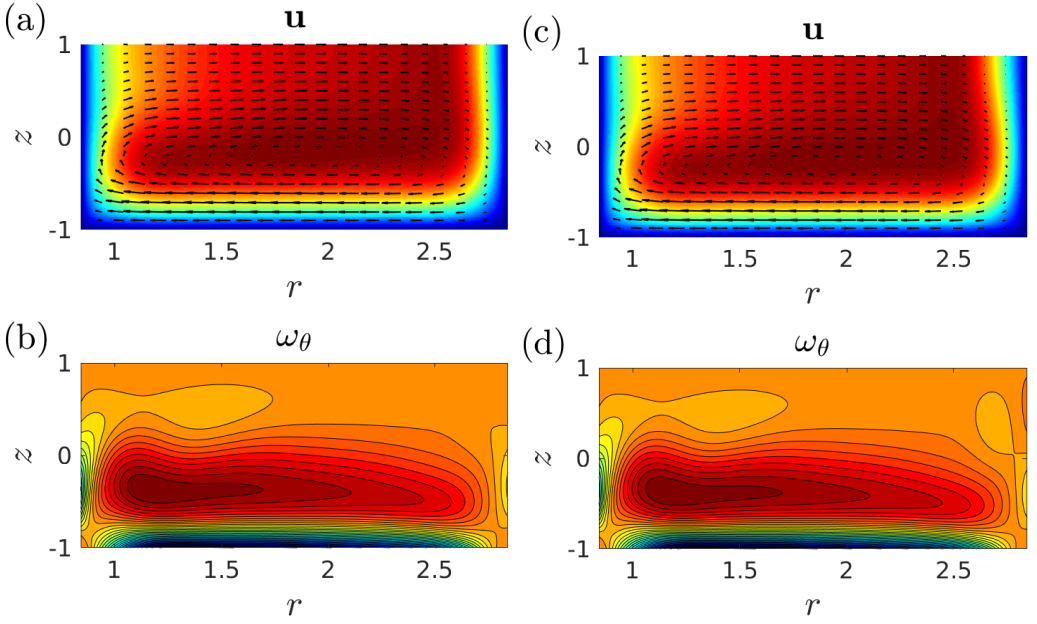

here, they are remarkably similar to dynamically forced flows reported by McCS, the appearance of which was due to the variation of the Lorentz force quantified by the Reynolds number. Both Type 1 and Type 2 solutions can co-exist in relatively thin layers for $0.219 \approx \epsilon_* < \epsilon < \epsilon_{**} \approx 0.261$ but they become topologically indistinguishable at $\epsilon = \epsilon_{**}$, as illustrated in Figure 3, and both cease to exist for $\epsilon > \epsilon_{**}$.

The subsequent analysis follows similar steps to those of McCS but explores the stability of the two steady axisymmetric solutions when the aspect ratio of the layer is varied while the total current flowing between the electrodes (i.e., dynamic forcing) remains fixed.

3 Linear stability analysis

We investigate the linear stability of the steady axisymmetric basic flow $\boldsymbol{w}_0 = [u_0, v_0, w_0, p_0]$ with respect to infinitesimal disturbances that are assumed to be periodic in θ. The velocity and pressure perturbations are written in a normal mode form as $\boldsymbol{w}_1(r,z)\exp(\sigma t + im\theta) + \text{c.c.}$, where $\boldsymbol{w}_1 = [u_1, v_1, w_1, p_1]$, c.c. denotes complex conjugate terms, and m is the circumferential wavenumber. Perturbations satisfy the following generalised eigenvalue problem for the complex temporal amplification rate $\sigma = \sigma^R + i\sigma^I$:

$$\begin{aligned}
\sigma u_1 = &-\partial_r p_1 + \left[\frac{1}{Re}\left(\partial_r^2 + \frac{1}{r}\partial_r - \frac{(1+m^2)}{r^2} + \frac{1}{\epsilon^2}\partial_z^2\right)\right. \\
&\left. - \frac{Ha^2 B_z^2}{\epsilon^2 Re} - u_0\partial_r - \partial_r u_0 - \frac{im v_0}{r} - w_0\partial_z\right] u_1 \\
&+ \frac{2}{r}\left[v_0 - \frac{1}{Re}\frac{im}{r}\right] v_1 + \left[\frac{Ha^2 B_r B_z}{Re} - \partial_z u_0\right] w_1\,, \qquad (13)\\
\sigma v_1 = &-\frac{im}{r} p_1 + \left[-\partial_r v_0 - \frac{v_0}{r} + \frac{1}{Re}\frac{2im}{r^2}\right] u_1 \\
&+ \left[\frac{1}{Re}\left(\partial_r^2 + \frac{1}{r}\partial_r - \frac{(1+m^2)}{r^2} + \frac{1}{\epsilon^2}\partial_z^2\right) - u_0\partial_r - \frac{im v_0}{r} - \frac{u_0}{r}\right. \\
&\left. - w_0\partial_z - \frac{Ha^2\left(\epsilon^2 B_r^2 + B_z^2\right)}{\epsilon^2 Re}\right] v_1 - \left[\partial_z v_0\right] w_1\,, \qquad (14)\\
\sigma w_1 = &-\frac{1}{\epsilon^2}\partial_z p_1 + \left[\frac{Ha^2 B_z B_r}{\epsilon^2 Re} - \partial_r w_0\right] u_1 - \left[\frac{im v_0}{r} + u_0\partial_r + \partial_z w_0 + w_0\partial_z\right. \\
&\left. - \frac{1}{Re}\left(\partial_r^2 + \frac{1}{r}\partial_r - \frac{m^2}{r^2} + \frac{1}{\epsilon^2}\partial_z^2\right) + \frac{Ha^2 B_r^2}{Re}\right] w_1\,, \qquad (15)\\
0 = &\left(\partial_r + \frac{1}{r}\right) u_1 + \frac{im}{r} v_1 + \partial_z w_1\,. \qquad (16)
\end{aligned}$$

The above eigenvalue problem is solved numerically. Figure 4(a) illustrates

Figure 4: (a) Linear amplification rate σ^R for $m = 0$. The lower branch (the dashed red line) corresponds to the Type 1 solutions that exists for $0 < \epsilon < \epsilon_{**} \approx 0.261$. The upper branch (the solid blue line) corresponds to the Type 2 solutions that exist for $0.261 \approx \epsilon_{**} > \epsilon > \epsilon_{*} \approx 0.219$. (b) The relationship between the aspect ratio and the Reynolds number for a fixed electric current.

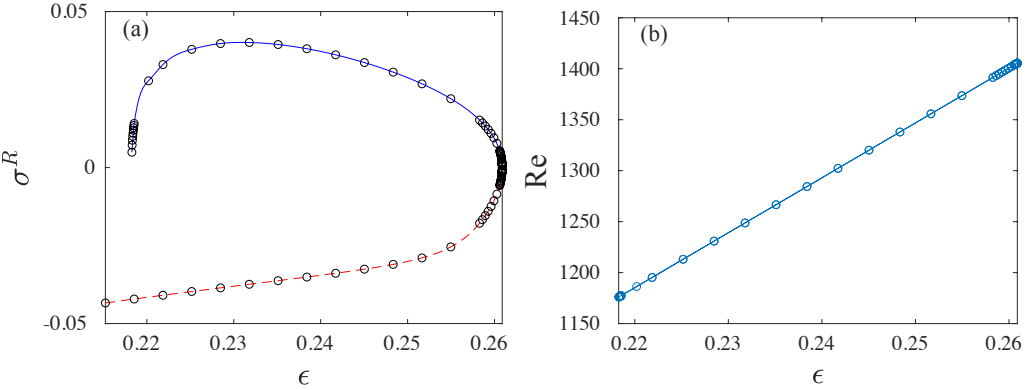

the real amplification rate σ^R as a function of the aspect ratio ϵ for $m = 0$. For small values of ϵ only the Type 1 solution exists, which is linearly stable ($\sigma^R < 0$). This remains so as ϵ increases until the layer reaches the critical thickness corresponding to $\epsilon = \epsilon_*$ and the Type 2 solution suddenly appears.

As ϵ increases further, the Type 1 solution remains stable while the σ^R values for the Type 2 solution become positive indicating their linear instability. At $\epsilon = \epsilon_{**}$ the σ^R values for both types of solutions approach zero, the lower and upper branches of the σ^R curve 'collide' and the toroidal structure near the outer wall disappears (Figure 3).

Despite being generated for fixed dynamic forcing, Figure 4(a) bears remarkable resemblance to the results reported by McCS for a variable Lorentz force. Figure 4(b) sheds light on the reason behind such an observation. The variation of the aspect ratio ϵ of the electrolyte layer when the total electric current flowing through it remains fixed leads to a proportional variation in

the Reynolds number Re that characterises the relative importance of the driving Lorentz force. Yet, the two physically distinct parameters are not equivalent in the sense that the critical values ϵ_* and ϵ_{**} computed here (limiting the existence range of Type 2 flows) cannot be rescaled to their Reynolds number counterparts Re_* and Re_{**} reported by McCS.

To investigate features of the instability further, in Figure 5 we present real amplification rates σ^R and the corresponding angular speeds $\omega = -\sigma^I/m$ of perturbations corresponding to systems with $m = 0, 1, \ldots, 9$ vortices. As seen from Figure 5(a), the $\sigma^R(\epsilon; m)$ are positive for Type 2 flows over different ϵ intervals. This signifies that the number of vortices observed experimentally depends on the depth of the layer. The modes with $m > 9$ have negative linear amplification rates and are not expected to be seen in experiments. The perturbation amplification rates for Type 1 solutions remain negative indicating that they are always stable. The $\sigma^R(\epsilon; m)$ curves translate downward as m increases and thus modes with larger numbers of vortices are less likely to be observed.

Plots in Figure 5(b) demonstrate that the angular wave speeds $\omega = -\sigma^I/m$ have close but distinct values across the vortex existence region. The exceptions are the $m = 1$ and $m = 2$ modes. The $m = 1, 2$ curves intersect the ones for larger values of m suggesting that a resonant interaction between the $m = 1, 2$ modes with the other modes can occur, although this cannot be confirmed within the framework of a linear stability analysis.

Recollect that the secondary toroidal structure in Type 2 flows induces a radial counterflow that results in a stagnation point $u_0 = 0$ at the free surface. Figure 6 shows that the absolute values of the free surface disturbance velocities (scaled by $\max\{|u_1|, |v_1|\}$) achieve their maxima at the same radial location in the close vicinity of the stagnation point separating the two tori. Therefore, vortex instability arises at the boundary between the large bulk toroidal flow structure and the smaller torus counter-rotating near the outer wall. This demonstrates that the existence of the secondary toroidal structure in Type 2 flow is the necessary condition for the onset of instability.

Figure 5: (a) Linear amplification rates σ^R for $m = 0$ ($\circ$), $m = 1$ ($+$), $m = 2$ ($*$), $m = 3$ ($\times$), $m = 4$ (square), $m = 5$ ($\diamond$), $m = 6$ ($\triangle$), $m = 7$ ($\triangledown$), $m = 8$ (hexagram) and $m = 9$ (pentagram). For Type 2 solutions (upper branches), $\sigma^R < 0$ for $m > 9$ and the corresponding curves are not shown. The lower branches corresponding to stable Type 1 solution are truncated to reduce clutter. (b) The corresponding angular speed $\omega = -\sigma^I/m$ for $m = 1, \cdots, 9$ ($\omega \equiv 0$ for $m = 0$).

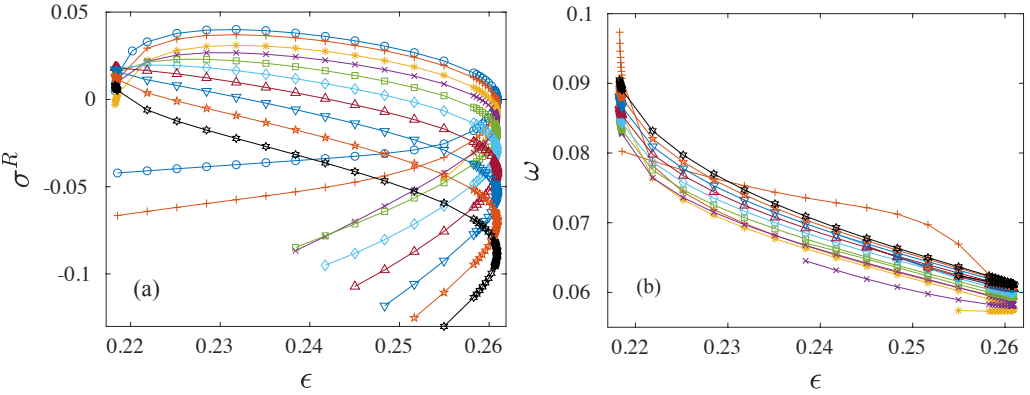

To obtain an insight into the mechanisms driving this instability, the balance of mechanical energy in the system is considered:

$$\sigma^R \Sigma_k = \Sigma_{vis} + \Sigma_{Ha} + \Sigma_{cc} + \Sigma_{bf}, \quad \text{where } \Sigma_X = \int_{-1}^{1} \int_{\alpha-1}^{\alpha+1} \Re\left(E_X\right) r \, dr dz, \quad (17)$$

where $\Re$ denotes the real part. Expressions E_X for $X = \{k, vis, Ha, cc, bf\}$ are derived from (13)–(15) multiplied by the complex conjugate eigenfunctions and represent: perturbation kinetic energy, viscous dissipation, electromagnetic effects, curvature effects, and interactions of perturbations with the basic flow, respectively, and are formally defined by McCS [2].

The kinetic energy term Σ_k is positively defined. Figure 7(a, b) compares the spatial fields of the basic flow ($E_{k,0}$) and disturbance (E_k) kinetic energy. The former is distributed throughout the r-z cross-section while the latter is

Figure 6: The perturbation velocities at the free surface for $\epsilon = 0.258$, $\mathrm{Ha} = 5.28 \times 10^{-3}$ and $\mathrm{Re} = 1391$ for (a, b) Type 1 and (c, d) Type 2 solutions. The vertical lines show the location of the stagnation point $r \approx 2.661$ of Type 2 flow at the free surface. Symbols are defined in Figure 5.

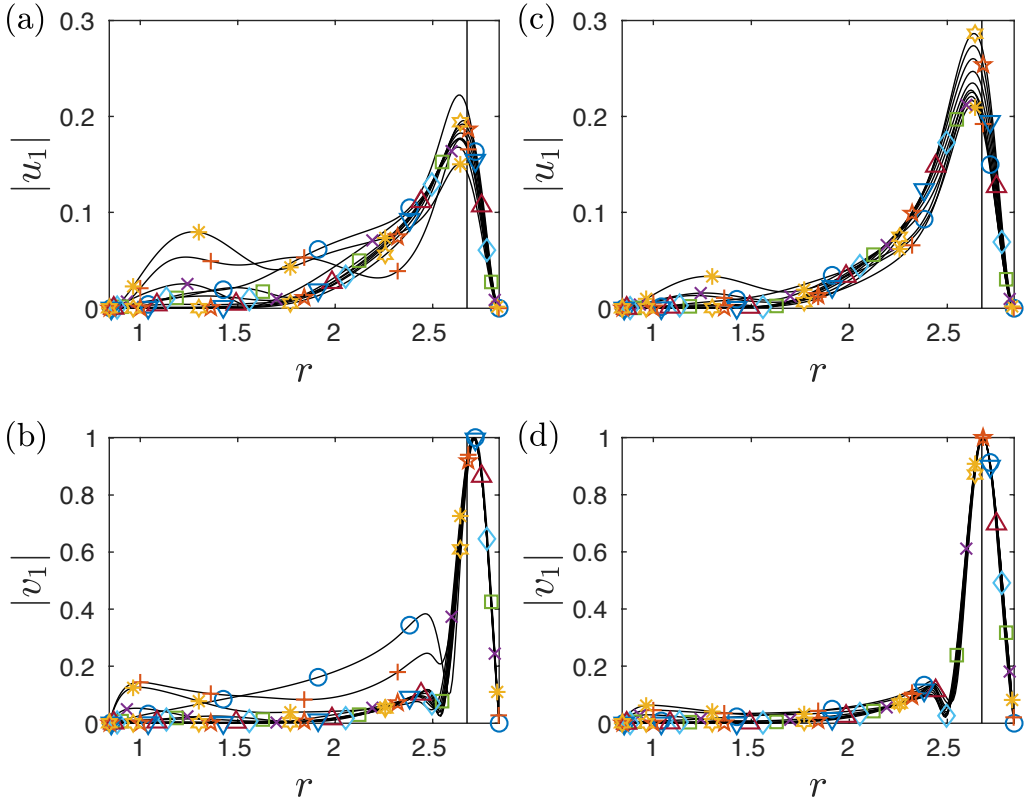

Figure 7: The r-z plane distributions of the basic flow kinetic energy $E_{k,0} = u_0^2 + v_0^2 + \epsilon^2 w_0^2$ and various perturbation energy integrands for the Type 2 basic flow solution with $m = 2$ for $\epsilon = \epsilon_* = 0.258$, $Ha = 5.28 \times 10^{-3}$ and $Re = 1391$.

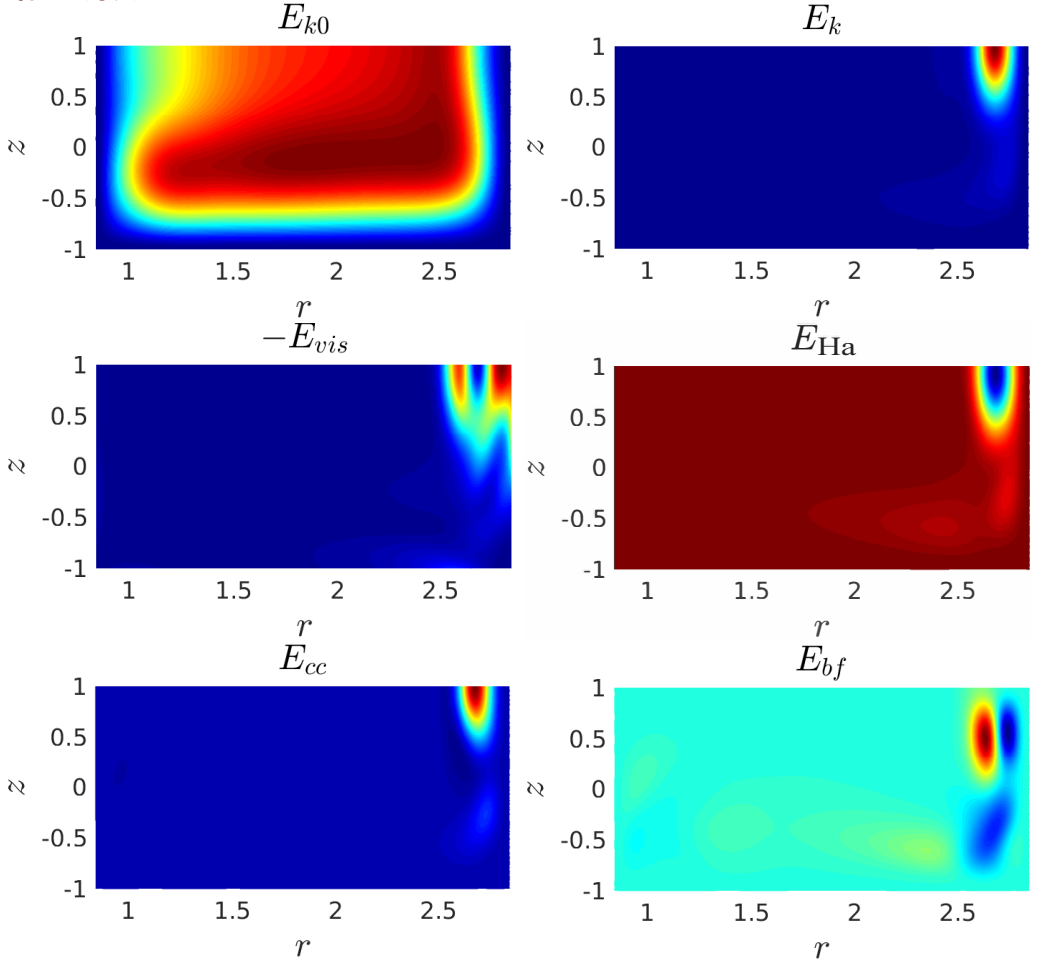

strongly localised near the free surface and the outer cylindrical wall where the vortices are seen. The vortices are formed in the region where the basic flow is less energetic and their occurrence reduces the kinetic energy deficit there. The sign of terms in the right-hand side of (17) differentiate between stabilising (negative) and destabilising (positive) influences. The viscous dissipation Σ_{vis} is negatively defined and is stabilising for all wavenumber $\mathfrak{m}$. The electromagnetic effects are characterised by consistently negative Σ_{Ha} and are stabilising but they are several orders of magnitude weaker than any other effects. Therefore, the Lorentz force, which drives the primary flow, makes a negligible contribution to the development of the instabilities. The effects of curvature and radial shear (including Rayleigh centrifugal destabilisation) Σ_{cc} and the energy exchange between the perturbations and the basic flow via non-radial shear Σ_{bf} are both positive and of the same order of magnitude, and thus both contribute to the instability.

The presented energy consideration for variable depth fluid layers is in agreement with McCS for variable forcing. Therefore, we conclude that in the considered problem the variation of independent dynamic and geometric parameters corresponding to two common experimental scenarios (variation of the Lorentz force and of the fluid depth) lead to a similar morphology of the experimentally observed flows. Furthermore, the current analysis demonstrates the robustness of the physical instability mechanism identified by McCS that remains unchanged in the two distinct physical scenarios: the observed vortices arise due to Rayleigh's inviscid centrifugal instability aided by radial shear in the boundary layer near the outer cylindrical wall, while the electromagnetic effects remain negligible.

Acknowledgements JMcC acknowledges support through the Australian Government Research Training Program Scholarship.

References

[1] P. A. Davidson. *An introduction to magnetohydrodynamics*. 2nd. Cambridge University Press, 2017. DOI: 10.1017/CBO9780511626333 (cit. on p. C217).

[2] J. McCloughan and S. A. Suslov. "Linear stability and saddle–node bifurcation of electromagnetically driven electrolyte flow in an annular layer". In: *J. Fluid Mech.* 887 (2020), A23.1–30. DOI: 10.1017/jfm.2020.29 (cit. on pp. C215, C217, C224).

[3] J. Pérez-Barrera, J. E. Pérez-Espinoza, A. Ortiz, E. Ramos, and S. Cuevas. "Instability of electrolyte flow driven by an azimuthal Lorentz force". In: *Magnetohydrodynamics* 51.2 (2015), pp. 203–213. URL: http://mhd.sal.lv/contents/2015/2/MG.51.2.4.R.html (cit. on p. C215).

[4] S. A. Suslov, J. Pérez-Barrera, and S. Cuevas. "Electromagnetically driven flow of electrolyte in a thin annular layer: Axisymmetric solutions". In: *J. Fluid Mech.* 828 (2017), pp. 573–600. DOI: 10.1017/jfm.2017.551 (cit. on p. C218).

Author addresses

1. **J. McCloughan**, Department of Mathematics, Swinburne University of Technology, Hawthorn, Victoria 3122, AUSTRALIA.
mailto:jmccloughan@swin.edu.au
orcid:0000-0001-8930-1552

2. **S. A. Suslov**, Department of Mathematics, Swinburne University of Technology, Hawthorn, Victoria 3122, AUSTRALIA.
mailto:ssuslov@swin.edu.au
orcid:0000-0002-0998-2712